



















Fe³⁺-hosting carbon phases in the deep Earth

Christian Albers ^{1,*}, Robin Sakrowski ¹, Lélia Libon ², Georg Spiekermann ³, Björn Winkler ⁴, Christian Schmidt ⁵,
Lkhamsuren Bayarjargal ⁴, Valerio Cerantola ⁶, Stella Chariton ⁷, Nico Giordano ⁸, Hlynur Gretarsson ^{8,9},
Johannes Kaa ^{1,6}, Hanns-Peter Liermann ⁸, Martin Sundermann ^{8,9}, Nicola Thiering ¹, Metin Tolan ¹, Max Wilke ²,
and Christian Sternemann ^{1,*}

¹Fakultät Physik/DELTA, Technische Universität Dortmund, 44227 Dortmund, Germany

²Institut für Geowissenschaften, Universität Potsdam, Karl-Liebknecht-Str. 24/25, 14476 Potsdam, Germany

³Institut für Geochemie und Petrologie, ETH Zürich, Clausiusstrasse 25, 8092 Zürich, Switzerland

⁴Institut für Geowissenschaften, Goethe-Universität Frankfurt, Altenhöferallee 1, 60438 Frankfurt am Main, Germany

⁵Deutsches GeoForschungsZentrum GFZ, Telegrafenberg, 14473 Potsdam, Germany

⁶European X-Ray Free-Electron Laser Facility GmbH, Holzkoppel 4, 22869 Schenefeld, Germany

⁷Bayerisches Geoinstitut, University of Bayreuth, 95447 Bayreuth, Germany

⁸PETRA III, Deutsches Elektronen-Synchrotron DESY, Notkestraße 85, 22607 Hamburg, Germany

⁹Max Planck Institute for Chemical Physics of Solids, 01187 Dresden, Germany



(Received 2 November 2021; revised 28 January 2022; accepted 3 February 2022; published 28 February 2022)

Iron-bearing carbonates play an important role in Earth's carbon cycle. Owing to their stability at mantle conditions, recently discovered iron carbonates with tetrahedrally coordinated carbon atoms are candidates for carbon storage in the deep Earth. The carbonates' iron oxidation and spin state at extreme pressure and temperature conditions contribute to the redox conditions and element partitioning in the deep mantle. By laser heating FeCO₃ at pressures of about 83 GPa, Fe₄³⁺C₃O₁₂ and Fe₂²⁺Fe₂³⁺C₄O₁₃ were synthesized and then investigated by x-ray emission spectroscopy to elucidate their spin state, both *in situ* and temperature quenched. Our experimental results show both phases in a high-spin state at all pressures and over the entire temperature range investigated, i.e., up to 3000 K. The spin state is conserved after temperature quenching. A formation path is favored where Fe₄³⁺C₃O₁₂ forms first and then reacts to Fe₂²⁺Fe₂³⁺C₄O₁₃, most likely accompanied by the formation of oxides. Density functional theory calculations of Fe₂²⁺Fe₂³⁺C₄O₁₃ at 80 GPa confirm the experimental findings with both ferric and ferrous iron in high-spin state with antiferromagnetic order at 80 GPa. As the intercrystalline cation partitioning between the Fe-bearing carbonates and the surrounding perovskite and ferropiclate depends on the spin state of the iron, an understanding of the redox conditions prevalent in subducted slab regions in the lower mantle has to take the latter into account. Especially, Fe₂²⁺Fe₂³⁺C₄O₁₃ may play a key role in subducted material in the lower mantle, potentially with a similar role as silicate perovskite.

DOI: [10.1103/PhysRevB.105.085155](https://doi.org/10.1103/PhysRevB.105.085155)

I. INTRODUCTION

Iron-bearing carbonates are important for chemical processes in the Earth's lower mantle and thus for understanding the deep carbon cycle [1]. Subduction of carbon-bearing phases (overwhelmingly carbonates) contained in descending slabs of oceanic crust are not only transported down to the transition zone but also to the Earth's lower mantle [2,3]. Carbonate inclusions found in diamonds formed at depths greater than 700 km demonstrate the occurrence of carbonates in deep mantle mineral assemblages [4–6]. To understand the stability of carbonates, numerous studies have been conducted from ambient to high-pressure-high-temperature (HPHT) conditions. These investigations allowed us to derive an understanding of pressure-induced structural phase transitions and changes in the structure-property relations and the electronic state, depending on thermodynamic conditions and composition [7–15]. Only recently has it

been shown that carbonates in which carbon is tetrahedrally coordinated by oxygen atoms, i.e., *sp*³-hybridized carbon, are stable at high pressures [16–25]. Specifically, at conditions prevalent in the deeper mantle with pressures >50 GPa, siderite (FeCO₃) transforms via self-oxidation-reduction reactions into new phases containing *sp*³ carbon [19–22]. These phases are candidates for the carbon transport to the core-mantle boundary. Although the structures of iron-bearing carbonates with tetrahedrally coordinated carbon are well characterized, information on their electronic structure is scarce. Cerantola *et al.* [22] demonstrated experimentally that either tetrairon(III) orthocarbonate (Fe₄³⁺C₃O₁₂), where only ferric iron is present, or diiron(II) diiron(III) tetracarbonate (Fe₂²⁺Fe₂³⁺C₄O₁₃), containing a mixture of ferric and ferrous iron, form. They predicted that the electronic configuration of iron in both phases is in the high-spin state, as the distance between iron and oxygen atoms is indicative of ferrous and ferric iron complexes in a high-spin state [26,27]. This is in contrast to siderite, which is in the low spin state at pressures >43 GPa. The oxidation state was deduced from charge balance considerations. The alternative is that Fe₂²⁺Fe₂³⁺C₄O₁₃ may be in an intermediate valence state (between 2⁺ and 3⁺),

*Corresponding authors: christian2.albers@tu-dortmund.de and christian.sternemann@tu-dortmund.de

TABLE I. List of sample conditions. Gray phases are not unambiguously verified at given conditions.

Sample	Pressure/ GPa	Temperature / K	Reaction product
A	80 ± 2	2700 ± 300	$\text{Fe}_4\text{C}_3\text{O}_{12}$, $\text{Fe}_4\text{C}_4\text{O}_{13}$
B	83 ± 2	3000 ± 200	$\text{Fe}_4\text{C}_4\text{O}_{13}$
C	82 ± 2	1700 ± 300 (<i>in situ</i>)	$\text{Fe}_4\text{C}_3\text{O}_{12}$, $\text{Fe}_4\text{C}_4\text{O}_{13}$
		2000 ± 300 (<i>in situ</i>)	$\text{Fe}_4\text{C}_3\text{O}_{12}$, $\text{Fe}_4\text{C}_4\text{O}_{13}$
		2600 ± 300 (<i>in situ</i>)	$\text{Fe}_4\text{C}_3\text{O}_{12}$, $\text{Fe}_4\text{C}_4\text{O}_{13}$
		3000 ± 300	$\text{Fe}_4\text{C}_3\text{O}_{12}$, $\text{Fe}_4\text{C}_4\text{O}_{13}$
D (SM) [39]	85 ± 2	2300 ± 200	$\text{Fe}_4\text{C}_3\text{O}_{12}$, $\text{Fe}_4\text{C}_4\text{O}_{13}$
		2800 ± 200	$\text{Fe}_4\text{C}_3\text{O}_{12}$, $\text{Fe}_4\text{C}_4\text{O}_{13}$

as the coordination polyhedra around the iron atoms are quite similar. Mössbauer spectroscopy measurements by Cerantola *et al.* [22] support the prediction of $\text{Fe}_4\text{C}_3\text{O}_{12}$ in a high-spin state, but an unambiguous determination of the spin state was prevented by the presence of further iron-containing phases. Recent density functional theory (DFT) calculations by Li and Stackhouse [28] indicated that $\text{Fe}_4\text{C}_3\text{O}_{12}$ is in a high-spin state at lower mantle pressures. As both phases are potential hosts for ferric iron in the deep Earth, they may affect the $\text{Fe}^{3+}/\Sigma\text{Fe}$ ratio, which is otherwise solely constrained by iron oxide phases and silicate perovskite [29–35]. The spin state influences the iron concentration in these structures. Studies have shown that the high spin to low spin transition impacts the iron partitioning and that low spin complexes bear higher iron contents. In other words, high-spin iron is more likely to be substituted by other elements [34,36–38]. The most important candidates for iron substitution are magnesium for ferrous and aluminum for ferric iron. The role of aluminum is of high interest in these depths, as it also may impact the enrichment of ferric iron in silicate perovskite, the most abundant phase in the deep Earth [30,31,34,36]. Hence, information on iron's oxidation and spin state in lower mantle phases is required to understand the chemical dynamics of subducted material in the Earth's mantle. In this paper, we determine the spin state of $\text{Fe}_4\text{C}_3\text{O}_{12}$ and $\text{Fe}_4\text{C}_4\text{O}_{13}$ obtained from single crystalline siderite in samples temperature quenched at high pressure and *in situ* at HPHT conditions. We explore a pressure and temperature range where former experiments have reported the appearance of these phases in the vicinity of the Earth's geotherm in the lower mantle regime. These conditions are achieved by the use of laser-heated diamond anvil cells (DACs). We exploit $K\beta_{1,3}$ x-ray emission spectroscopy (XES) with a spatial resolution of $8 \mu\text{m}$ for spin-state imaging of temperature quenched and *in situ* heated samples at high pressure. Complementary structural information is achieved with optical Raman spectroscopy and x-ray diffraction (XRD) by scanning the samples with a spatial resolution of $2 \mu\text{m}$. Thus, we are able to assign the information about the spin state to specific crystalline phases. We find that iron is in the high-spin state in both sp^3 carbonates over the entire temperature range. DFT calculations support this finding for diiron(II) diiron(III) tetracarboxate.

II. RESULTS

In the following, we present the experimental results and calculations and discuss their implication for the iron's spin state in tetrairon(III) orthocarbonate and diiron(II) diiron(III)

tetracarboxate. Overall, we discuss four different samples to disentangle information of tetrairon(III) orthocarbonate (A and C) and diiron(II) diiron(III) tetracarboxate (B and C) based on temperature quenched and *in situ* (C) measurements. Sample D contains both phases and is presented in the Supplemental Material (SM) [39]. An overview of the sample conditions is listed in Table I. All samples were measured at high pressure.

A. Tetrairon(III) orthocarbonate

All references in this paragraph refer to Fig. 1. The characterization by Raman spectroscopy was performed at the heated side of the sample. The corresponding results presented in Fig. 1(a) show that most of the sample contains siderite (blue), but low wave-number Raman bands appear for wave numbers between 130 and 300 cm^{-1} , ranging from the center to the left side of the sample (green). The comparison with the XRD data [see Fig. 1(b)] confirms the spatial distribution of siderite (blue) and indicates the appearance of $\text{Fe}_4\text{C}_4\text{O}_{13}$ (green) in the same region where low wave-number Raman bands were observed. Furthermore, $\text{Fe}_4\text{C}_3\text{O}_{12}$ (red) is present on the leftmost side of the sample as the dominating phase and at a small spot in the center of the sample. In Figs. 1(c) and 1(d), we show Raman spectra and diffraction patterns, respectively, for a traverse across the sample indicated by the arrow in Fig. 1(b). From the left to the right part of the sample [bottom to top in Figs. 1(c) and 1(d)] the diffraction patterns show a dominating contribution by $\text{Fe}_4\text{C}_3\text{O}_{12}$ (red), followed by pure siderite (blue) while $\text{Fe}_4\text{C}_4\text{O}_{13}$ (green) can be identified in the intermediate region. The spatial variations observed in the Raman spectra nicely correlate with those of the diffraction analysis. XES imaging clearly identifies different spin states of iron across the sample. Changes in the iron's $K\beta$ line shape are visualized in Fig. 1(e) for the same traverse discussed above. The corresponding total spin values are shown in Fig. 1(f). Overall, the integrated absolute difference (IAD) [40] and compositional fit analyses provide concurrent spin values. Both analyses show the same changes from a higher to lower spin value. The two-dimensional spin map in (g) extends the information from Fig. 1(f) to the whole sample. There is a low-spin regime on the right-hand side and a high-spin regime on the left-hand side in which we observe $\text{Fe}_4\text{C}_3\text{O}_{12}$ and a low amount of $\text{Fe}_4\text{C}_4\text{O}_{13}$. Compared to the center, the rim of the map is based on a much lower XES intensity and thus has a larger uncertainty of the spin values [see spectra in (e)]. For comparison, we calculated a spin map based on the XRD map supposing a spin value of

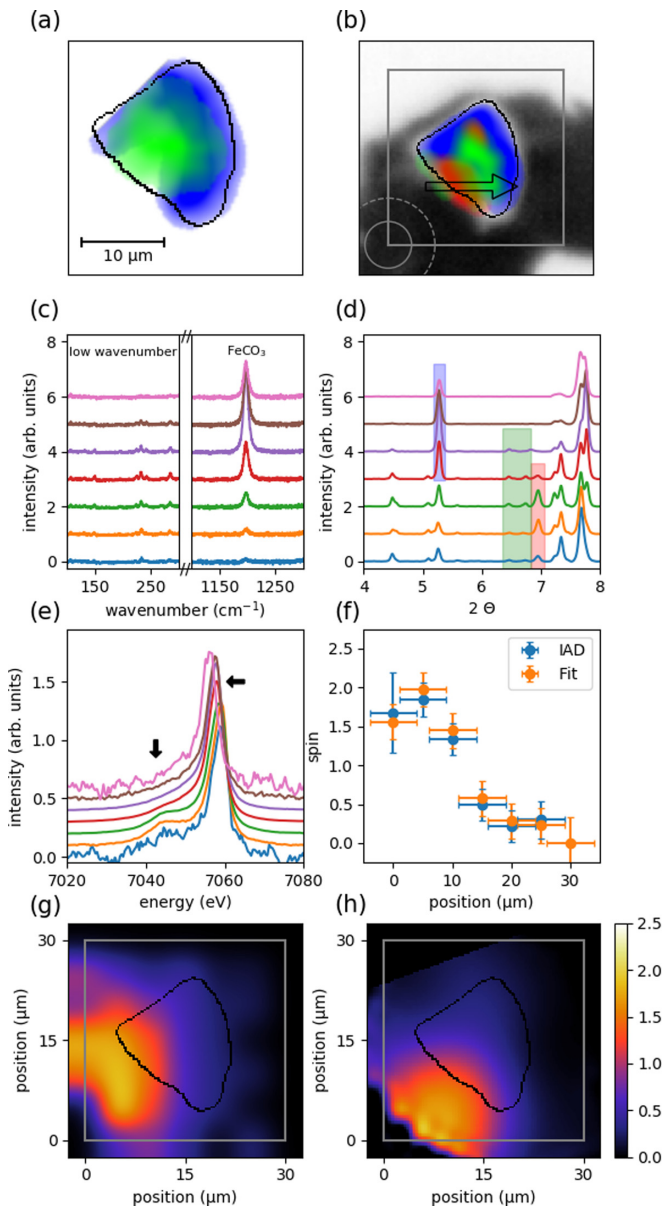


FIG. 1. Imaging results for sample A. (a) Raman map for FeCO_3 (blue) and the low wave-number bands (green). (b) Photo of the sample with the spatial distribution of FeCO_3 (blue), $\text{Fe}_4\text{C}_3\text{O}_{12}$ (red), and $\text{Fe}_4\text{C}_4\text{O}_{13}$ (green) revealed by XRD imaging. In black, the contour of the sample is visualized. The grey square marks the scanning region for XES imaging and matches the squares shown in (g) and (h). The grey circles indicate the intensity of the x-ray beam during XES measurements for 50% (solid, corresponding to $8\ \mu\text{m}$ FWHM) and 5% (dashed) intensity. The black arrow visualizes the cross section probed in (c)–(f). (c) Raman spectra, (d) XRD pattern with shaded areas indicating the different phases using the same color code as in (b) (full size figure in SM [39]), (e) $\text{K}\beta$ -XES spectra, and (f) extracted spin values following the black arrow from (b). The cross section from left to right corresponds to spectra from bottom to top in (c)–(e). (g) Spin map based on the XES analysis using IAD. Due to the low intensity, values on the rightmost side were set to zero manually. (h) Spin-state map of the sample derived from the XRD map (see text for details).

2.5 for $\text{Fe}_4\text{C}_3\text{O}_{12}$, shown in Fig. 1(h). The contribution of $\text{Fe}_4\text{C}_4\text{O}_{13}$ was neglected for this map as the XRD data imply

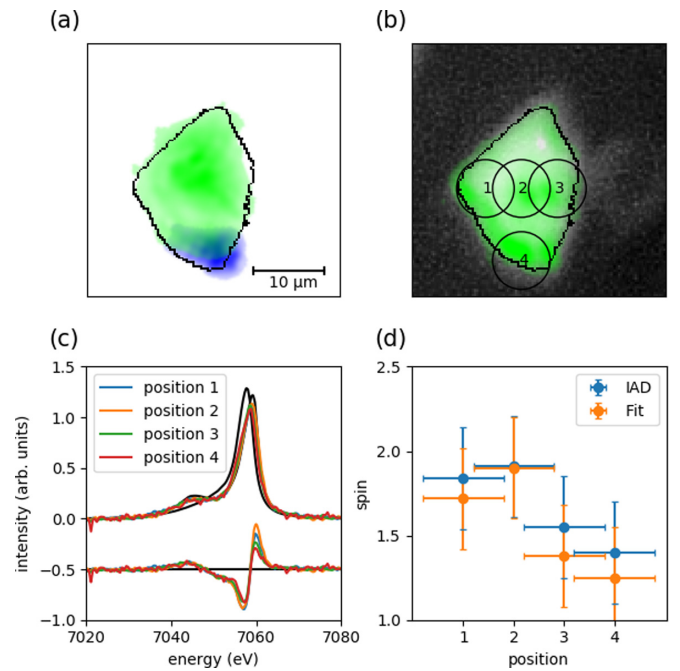


FIG. 2. Imaging results for sample B. (a) Raman map for FeCO_3 (blue) and the low wave-number bands (green). (b) Picture of the sample with the spatial distribution of $\text{Fe}_4\text{C}_4\text{O}_{13}$ (green), analyzed by XRD. In black, the contour of the sample is shown. The circles mark the areas where XES spectra were taken. (c) XES spectra of the different positions. The black spectra correspond to reference spectra for spin 0 and 2. (d) Spin values calculated by IAD for all spots from (b).

that its concentration is lower by a factor of 10 compared to $\text{Fe}_4\text{C}_3\text{O}_{12}$. As no powder average was measured, it is not possible to quantify the exact amount of the emerging phases by XRD. Therefore, the $\text{Fe}_4\text{C}_3\text{O}_{12}$ contribution was weighted arbitrarily with a factor of 3 compared to siderite. Despite the deficiencies of this analysis and considering the very different spatial resolution of the measurements, we find a reasonable agreement between the spin maps. To conclude, all presented maps are in mutually good agreement and show a consistent distribution of the crystalline phases and spin distribution. This leads us to conclude that $\text{Fe}_4\text{C}_3\text{O}_{12}$ is in a high-spin state. The spin state of $\text{Fe}_4\text{C}_4\text{O}_{13}$ could not be determined in this sample but will be discussed in the following.

B. Diiron(II) diiron(III) tetracarbonate

Raman spectroscopy imaging in Fig. 2(a) shows that most of the sample's siderite decomposed upon heating. Only a small amount remains in the lower part of the sample. The majority of the map shows low wave-number Raman bands as discussed before. XRD imaging [Fig. 2(b)] confirms the absence of siderite in most of the sample. In fact, due to the proximity of siderite Bragg reflections to those of $\text{Fe}_4\text{C}_4\text{O}_{13}$ and argon, no clear siderite signal could be extracted from the data within the limits of this analysis. The majority of the sample contains $\text{Fe}_4\text{C}_4\text{O}_{13}$ as a crystalline reaction product, while the appearance of oxides, as predicted by Cerantola *et al.* [22], cannot be excluded unambiguously due to the complexity of the diffraction pattern due to the dominating contributions

from $\text{Fe}_4\text{C}_4\text{O}_{13}$ and argon. To explain the Raman signal, we performed measurements for the most abundant iron oxides, FeO , Fe_2O_3 , and Fe_3O_4 , and observed no Raman bands at a pressure of 75(2) GPa in the wave-number range from 100 cm^{-1} to 1300 cm^{-1} . Thus, we can exclude these crystalline phases as possible candidates for the low wave-number bands while their occurrence is strongly correlated to the appearance of $\text{Fe}_4\text{C}_4\text{O}_{13}$ based on the XRD imaging results. Hence, the low wave-number Raman bands might be assigned either to $\text{Fe}_4\text{C}_4\text{O}_{13}$ or iron oxides, which are discussed in more detail in the computational results. XES spectra were taken at selected points on the sample as indicated in Fig. 2(b) and are visualized in Fig. 2(c). The geometry of the cell only allowed for XES data acquisition in forward scattering. Thus, the data quality is not as high as in the previous sample. However, the XES spectra show a clear distinction to the low-spin reference. IAD as well as compositional fit analysis show similar spin values for all spots [Fig. 2(d)]. Although the uncertainty in the values is relatively high, it is clear that all spectra show a large proportion of high-spin iron. If the prediction of Cerantola *et al.* [22] for $\text{Fe}_4\text{C}_4\text{O}_{13}$ is correct, the total spin value of the formation pathway would be ~ 1.8 , assuming Fe_2O_3 in the low spin state, which is in reasonable agreement with our results.

C. Tetrairon(III) orthocarbonate and Diiron(II) diiron(III) tetracarboxate - *in situ* measurements

XES imaging was performed *in situ* at high temperatures. The heating procedure lasted around 25 minutes for each measured spin map at different temperatures ranging from 1700 K

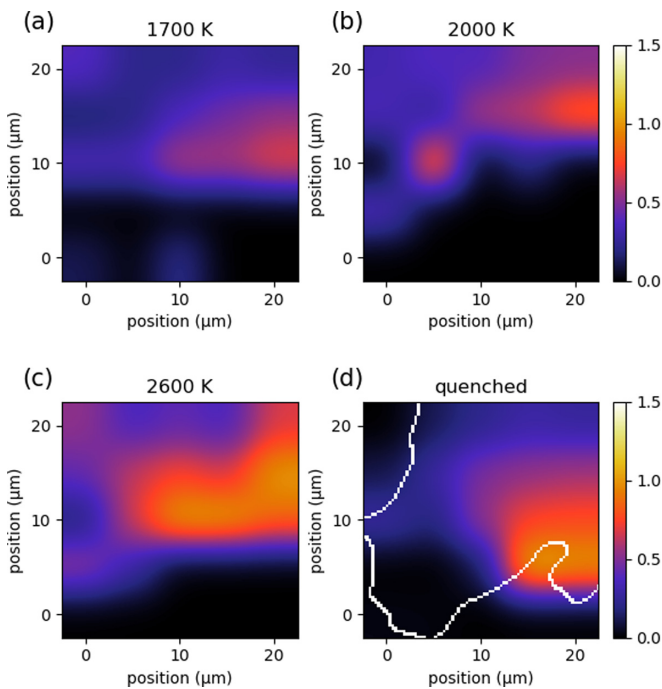


FIG. 3. *In situ* and *ex situ* spin maps for sample C. Spin maps for (a) 1700 K, (b) 2000 K, and (c) 2600 K. The XES measurements were performed under *in situ* conditions. (d) Spin map after temperature quenching the sample with the contour of the sample in white. Due to the cooling process after heating, the sample position slightly changed.

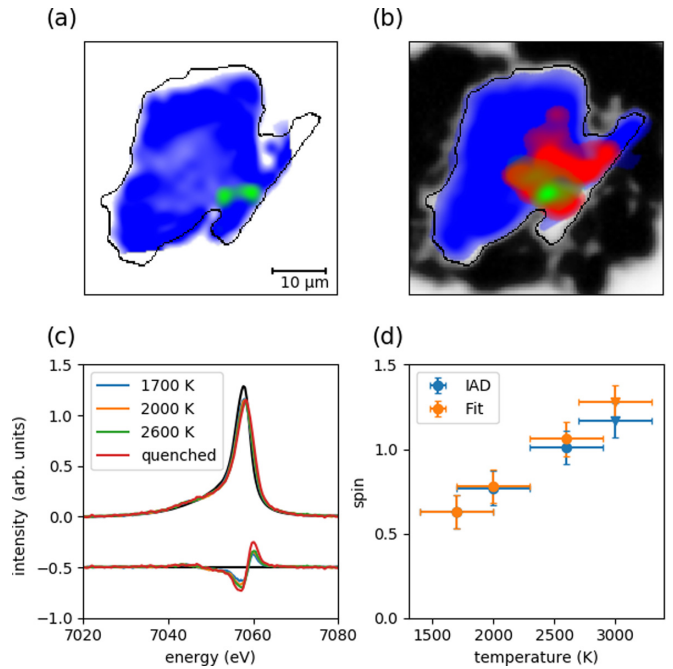


FIG. 4. Imaging results for sample C after temperature quenching. (a) Raman map for FeCO_3 (blue) and the low wave-number bands (green). (b) Picture of the sample with colors indicating the position of the remaining FeCO_3 (blue) and the emerged $\text{Fe}_4\text{C}_3\text{O}_{12}$ (red) and $\text{Fe}_4\text{C}_4\text{O}_{13}$ (green), analyzed by XRD. In black, the contour of the sample is shown. (c) XES spectra with the maximum spin value for each *in situ* measurement and the quenched spectrum: The differences to the low spin reference (black) are underneath the spectra. (d) Maximum spin values calculated by IAD for all *in situ* measurements and the quenched one (triangle). The quenched spectra are set to 3000 K, as this was the maximum temperature during the whole heating process.

to 2600 K and around four hours in total. The highest sample temperature was 3000 K, which was not measured *in situ* by XES imaging. The spin maps are presented in Fig. 3 and show an increasing high-spin contribution while measuring at high temperatures [Figs. 3(a)–3(c)]. The variation in position of the area with high-spin contribution, especially after temperature quenching the sample, is due to slight variations of the sample position due to heating. Notably, the high spin contribution present in the *in situ* measurements is conserved in the cold sample [see Fig. 3(d)]. In Fig. 4(c), we present the XES spectra indicating the highest spin state measured during *in situ* imaging. For all temperatures, an increase in the spin values was observed. Even at the lowest temperature of 1700 K, there is a clear difference to the low spin reference. With increasing temperature, the spin values rise further [Figs. 4(c) and 4(d)]. After temperature quenching, the spin value is slightly higher than during heating, which we trace back to the slight sample movements during *in situ* data acquisition, i.e., larger contribution of siderite to the spectra. The phase distribution determined by Raman spectroscopy and XRD [Figs. 4(a) and 4(b)] show the presence of mostly $\text{Fe}_4\text{C}_3\text{O}_{12}$, accompanied by a small area containing $\text{Fe}_4\text{C}_4\text{O}_{13}$. Again low wave-number Raman bands are detected in this area. Their spatial distribution agrees well with the results

TABLE II. Lattice parameters of Fe₄C₄O₁₃ at high pressures from experiment and DFT calculations.

	$a / \text{\AA}$	$b / \text{\AA}$	$c / \text{\AA}$	$\beta / [^\circ]$	$V / \text{\AA}^3$
85 GPa (exp)	10.36(2)	4.015(20)	13.605(50)	107.85(20)	538.66(5.00)
85 GPa (DFT)	10.3918	4.0485	13.5602	106.98	545.62
97 GPa (exp) [22]	10.261(3)	3.985(3)	13.455(5)	107.85(4)	523.76(28)
97 GPa (DFT)	10.3161	4.0149	13.478	107.04	533.72

from XES imaging. Thus, we can conclude that iron in both carbonates with tetrahedrally coordinated carbon is in the high spin state over the entire temperature range probed here. The total spin values are relatively low compared to the previously presented samples. This is due to the presence of a non-negligible amount of unreacted siderite. Both XRD as well as Raman spectroscopy imaging indicate siderite in all parts of the sample. Thus, the area probed by XES always contains a mixture of siderite and predominantly Fe₄C₃O₁₂. This is confirmed by XES maps deduced from the XRD results (see SM [39] Fig. S7). Based on the *in situ* results, we infer that Fe₄C₃O₁₂ is first formed at a temperature of 1700 K and reacts at higher temperature to form Fe₄C₄O₁₃. This is consistent with the relatively low amount of Fe₄C₄O₁₃ that appears in the center of the heating spot. These p-T conditions are in accordance with the literature [22,28]. With increasing temperature, the heated area increases due to small movements of the cell and the increasing temperature gradient. Thus, the amount of transformed siderite increases, which is in accordance with the increasing area with a spin value > 0 for the XES imaging.

D. Computational results

DFT calculations of Fe₄C₃O₁₂ by Li and Stackhouse [28] find iron to be in the high-spin state at conditions of the mantle geotherm, which is confirmed by our experimental results. However, in the study of Li and Stackhouse, results on Fe₄C₄O₁₃ were not reported. Hence, we performed DFT calculations on Fe₄C₄O₁₃ at high pressures, which confirmed that the ground-state structure is an antiferromagnetic high-spin structure. A comparison of experimentally determined lattice parameters at 97 GPa [22] and at 85 GPa (Table II) to those obtained here by DFT calculations show a very satisfactory agreement with differences $< 2\%$, where the DFT-GGA-PBE+*U* calculations slightly overestimate the lattice parameters due to the commonly encountered under-binding. Calculations in which a low spin state was imposed gave too small lattice parameters, which differed markedly from the experimental values. Similar to recent results on other carbonates in which the carbon is fourfold coordinated by oxygen [24,25], the DFT calculations show that all C–O bonds are covalent, with bond populations ranging from 0.8–0.6 $e^-/\text{\AA}^3$. The carbon atoms are therefore tetrahedrally coordinated by oxygen and thus sp^3 hybridized. In Fe₄C₄O₁₃, the CO₄⁴⁻-groups are polymerized by corner-sharing into C₄O₁₃¹⁰⁻ entities. The C–O bonds between the carbon atoms and those oxygen atoms which are corner-shared are systematically longer (~ 1.40 \AA) than the C–O bonds to the nonshared oxygens (~ 1.28 – 1.36 \AA). A Mulliken population analysis showed a clear difference between Fe²⁺ and Fe³⁺, as the former had a Mulliken charge of 1.22 e^- while the latter

had a charge of 1.42 e^- . It should be noted that Mulliken population analyzes typically give values of close to half the formal charge. The spin state associated with the iron ions would be 4 $\hbar/2$ for high spin $3d^6$ -Fe²⁺ and 5 $\hbar/2$ for $3d^5$ -Fe³⁺ in octahedral coordination. The Mulliken values are $-3.6 \hbar/2$ and $4.02 \hbar/2$, respectively, and hence the ground state structure at 80 GPa in the athermal limit is antiferromagnetic high spin. The intense experimentally observed Raman signal is indicative for the presence of a band gap, as metals typically yield no Raman signal. The DFT calculations gave band gaps only for the high-spin calculations. DFT-GGA-PBE are known to systematically yield too small band gaps, so the band gap computed here at 85 GPa (~ 0.5 eV) is likely a lower limit. As siderite crystallizes in a centrosymmetric space group, Raman active modes cannot be IR active and vice versa. The theoretical spectra clearly show that at 80 GPa there are no modes at the Γ point with energies < 350 cm⁻¹ and in fact there are only four E_g and one A_{1g} modes which have measurable intensities, all of which have Raman shifts > 450 cm⁻¹ [see Fig. 5(a)], which is supported by various

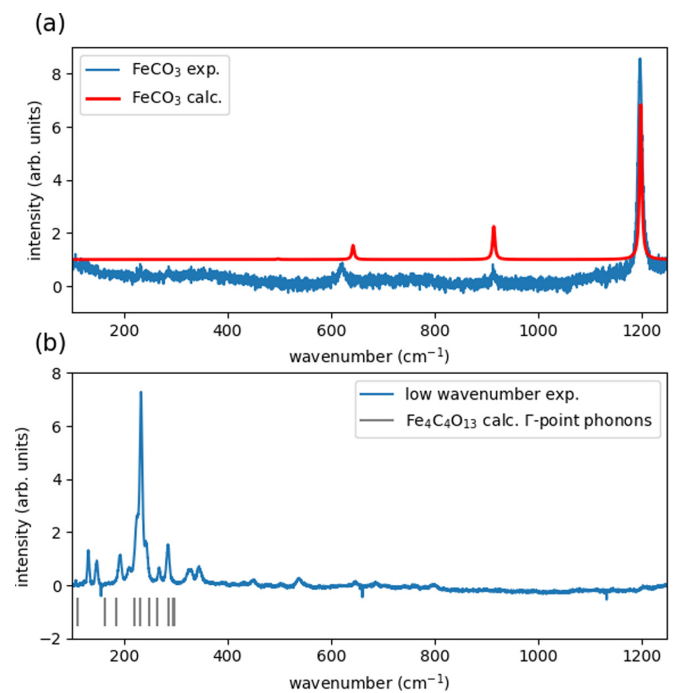
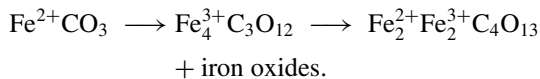


FIG. 5. High-pressure Raman spectra. (a) Experimental Raman spectra for siderite as well as calculated Raman spectra at 80 GPa. (b) Low wave-number Raman bands and Raman shifts of low wave-number Raman active modes at the Γ point for Fe₄C₄O₁₃ are shown. These are only a selection of all active Raman modes to highlight the difference to the Raman spectrum of low-spin siderite.

experimental studies [7,8,10]. Currently, we cannot compute Raman intensities for spin-polarized DFT-GGA-PBE+ U calculations. Hence, we computed only the expected Raman shifts for $\text{Fe}_4\text{C}_4\text{O}_{13}$, to highlight the differences of the low-frequency part of the Raman spectrum of low-spin siderite, which has no low-frequency Raman modes below 300 cm^{-1} , and $\text{Fe}_4\text{C}_4\text{O}_{13}$, which has numerous bands in that spectral region [see Fig. 5(b)].

III. IMPLICATIONS

The setup we utilized to synthesize and analyze the samples provides a wide range of opportunities to study the electronic structure for high pressure and high temperature studies, even under *in situ* conditions, for a variety of fields in material sciences. With this setup, we proved both iron-bearing phases with tetrahedrally coordinated carbon to be in a high-spin state, which is furthermore supported by DFT calculations for $\text{Fe}_4\text{C}_4\text{O}_{13}$. Although a detailed analysis of the samples is challenging due to their heterogeneity, Raman and XRD imaging with high spatial resolution in combination with XES imaging provides clear results. The temperatures at which we found both phases are in accordance with the observations by Cerantola *et al.* [22]. Especially, the phase distribution in sample C suggests that at lower temperatures, $\text{Fe}_4\text{C}_3\text{O}_{12}$ is formed, which reacts to $\text{Fe}_4\text{C}_4\text{O}_{13}$ only if the temperature is substantially increased. This is supported by an analysis of sample B which we CO_2 -laser heated to 3000 K. One might speculate that for sample D (SM [39]), $\text{Fe}_4\text{C}_3\text{O}_{12}$ emerges in the first heating process at 2300 K and $\text{Fe}_4\text{C}_4\text{O}_{13}$ in the second heating process at 2800 K. Our observations suggest the following formation pathway:



Although we cannot provide a stoichiometrically correct reaction equation based on our results, it is indisputable that in the second reaction iron-oxides have to form. Due to the complexity of Bragg reflections in the XRD imaging data, the composition and structures of these oxides remain unknown. Possible candidates are high-pressure phases such as FeO , Fe_2O_3 , $h\text{-Fe}_3\text{O}_4$, Fe_4O_5 , and higher order iron-oxides [27]. Another possibility is the recently discovered FeO_2 , as its stability field matches our experimental conditions [41]. Metallic iron (Fe^0) could also form as a product of the redox reaction, owing to its stability in the presence of bridgmanite, independently of oxygen fugacity [30]. Recently, it has been shown by Spahr *et al.* [25] that the stability conditions for tetrahedrally coordinated carbon phases can be shifted to lower pressures if oxide phases are present prior to the heating process. It is possible that their results on Sr_2CO_4 can be adapted to iron-bearing phases. Hence, both CO_4^{4-} containing phases in our study might stabilize at much shallower depths in the lower mantle, impacting the redox equilibrium that governs the stability of silicate perovskite and reduced iron-oxides species. Similarly to silicate perovskite, $\text{Fe}_2^{2+}\text{Fe}_2^{3+}\text{C}_4\text{O}_{13}$ contains iron in multiple valence states, as ferrous and ferric ions, thus at least locally we suggest it can play an important role as a redox buffer in deep mantle. Concerning the element partitioning, ferrous iron, preferentially in the high-spin

state, can be exchanged with magnesium ions. This process is particularly relevant when contextualized in the deep mantle, where low-spin ferropericlase due to the spin transition becomes progressively enriched in iron at the expenses of silicate perovskite and donating magnesium ions if the system is aluminium-free [34]. If the system contains aluminum, the mechanism behind the iron partitioning becomes more complex [34,36–38,42,43]. Shim *et al.* [43] report a reduction of Fe^{3+} content for silicate perovskite in a pressure range between 40–70 GPa, with a simultaneous increase of Fe^{2+} content in ferropericlase under strongly reducing conditions, whereas the Fe^{2+} in the silicate perovskite remains stable. At higher pressures, this effect is turned around and the Fe^{3+} content in silicate perovskite increases again on loss of Fe^{2+} in the ferropericlase. The drop in iron content in the silicate perovskite is explained by a change in the substitution mechanism from the charge-coupled combined substitution of aluminum and iron to a mechanism in which aluminum is incorporated on either of the distinct cation sites in the silicate perovskite structure. Piet *et al.* [34] reported the same effect but for a much higher pressure with a minimum in iron content at 85 GPa, a pressure close to our experimental conditions. They conclude that the total iron content in silicate perovskite is controlled by aluminum in the silicate perovskite and its decrease is explained with the onset of the high spin to low spin transition in the ferropericlase at 70 GPa. However, in a recent study, Huang *et al.* [44] emphasized the role of oxygen fugacity and typology of coexisting phases for iron partitioning in the lower mantle. As both of the phases with tetrahedrally coordinated carbon have shown to be stable at lower mantle conditions, they should be considered in the complex redox chemistry behind aluminium/magnesium exchange. Due to the increased ionic radius of high-spin iron compared to low-spin iron, substitution reactions of ferric (ferric/ferrous) iron in $\text{Fe}_4\text{C}_3\text{O}_{12}$ ($\text{Fe}_4\text{C}_4\text{O}_{13}$) are likely and can be of relevance in the understanding of redox equilibria with ferropericlase, silicate perovskite, and iron. To summarize, our study unambiguously confirms both investigated phases are in high-spin states for temperature-quenched samples as well as under *in situ* conditions. The observation of high-spin states under *in situ* conditions implies that our results are relevant for iron partitioning and complex redox chemistry in subducted material in the deep Earth. The experimental results are supported by DFT calculations of Li *et al.* [28] for $\text{Fe}_4\text{C}_3\text{O}_{12}$ and by our own calculations for $\text{Fe}_4\text{C}_4\text{O}_{13}$. Furthermore, our DFT calculations confirm the predictions of Cerantola *et al.* [22] of both ferrous and ferric iron in $\text{Fe}_2^{2+}\text{Fe}_2^{3+}\text{C}_4\text{O}_{13}$. Thus, substitution of iron by magnesium and aluminum is more favorable than for low-spin iron complexes. For the magnesium substitution, this provides a new reservoir of ferrous iron and vice versa. Furthermore, the ferric iron polyhedra in both reported phases can host aluminum. This may influence the iron partitioning in ferropericlase and silicate perovskite systems in subducted slabs, which are the most abundant phases in the deep Earth.

IV. MATERIALS AND METHODS

The starting material for the synthesis of tetrairon(III) orthocarbonate and diiron(II) diiron(III) tetracarbonate was single-crystalline siderite (FeCO_3) (synthesis process

described by Cerantola *et al.* [9]) with a size of 15 μm –30 μm in diameter and a thickness of ~ 15 μm , which was pressurized to about 80 GPa. The pressure was applied by a DAC with argon [neon for sample D (SM [39])] as a pressure-transmitting medium to ensure quasihydrostatic conditions. The samples were loaded without an additional laser absorber [45]. The pressure was determined by optical Raman spectroscopy [46]. Rhenium foil with a thickness of ~ 200 μm was used as a gasket material. We employed different DACs for the experiments. The details are given in Table S1 [39,47,48]. To maximize the signal from the sample, a special gasket preparation was developed and applied for samples A and C, which allowed for a horizontal scattering angle of $\sim 70^\circ$. The exact procedure is described in the SM [39]. All samples were laser heated at high pressure. Samples A, C, and D (SM [39]) were heated with a Yb:YAG-Laser [49] and a wavelength of ~ 1 μm , either at the University of Potsdam or at beamline P01 at Deutsches Elektronen Synchrotron (DESY). Sample B was heated at the University of Frankfurt with a CO₂ laser and a wavelength of ~ 10 μm . To confirm the formation of tetrahedrally coordinated carbonates, Raman spectroscopy and XRD were used. All measurements for phase characterization were performed after temperature quenching at high pressure. Optical Raman spectroscopy was performed at Deutsches GeoForschungsZentrum in Potsdam with a laser of 532-nm wavelength and ~ 2 μm spatial resolution. The Raman maps provide information about new crystalline phases in the sample and the position of the heating spot. For a full characterization of the newly formed phases, XRD imaging was performed at beamline P02.2 at DESY using a Perkin Elmer XRD 1621 detector with a pixel size of 200×200 μm^2 . The detector was calibrated using CeO₂ (NIST standard 647b). For sampling, a step size of 2 μm was used, resulting in 20×20 μm^2 – 40×40 μm^2 -sized XRD maps. The beam size was focused down to 2×2 μm^2 FWHM at 42.78 keV (0.2898 Å). To obtain information about the electronic structure, XES was used. The measurements were performed at beamline P01 at PETRA III, DESY. The beamsize was focused to 8×8 μm^2 using a Kirkpatrick-Beaz mirror system. The incident energy was fixed to 10.4 keV which is, on one hand, a good compromise between transmission through the upstream diamond and absorption of the sample and, on the other hand, prevents the appearance of Compton scattering, resulting in a reduced background. The beam was monochromatized by a Si(111) double crystal monochromator which resulted in a flux of $\sim 6 \times 10^{13}$ ph/s on the sample at given energy. The setup contains an energy dispersive von Hamos spectrometer [50,51], equipped with 4 Si(110) analyzer crystals with a bending radius of 500 mm [13], along with a Pilatus 100 K 2D detector with a pixel size of 172×172 μm^2 . To obtain the XES spectra, we used different geometries. The first one is in a 0° horizontal scattering angle, resulting in a total scattering angle of 23.8° (forward scattering), measuring the emission through the whole downstream diamond (samples B and D). The second one is in $\sim 70^\circ$ horizontal scattering geometry, resulting in a total scattering angle of 71.5° (near 90°), collecting the emission spectra in between cell and gasket (samples A and C). This has the great advantage of only passing ~ 0.5 mm of

TABLE III. List of reference samples.

Sample	Pressure / GPa	Spin
FeCO ₃	82.0	0.0
Fe ₂ O ₃	75.0	0.5
FeO	13.4	2.0
Fe ₂ O ₃	13.4	2.5

diamond instead of 2.2 mm, which increases the signal by a factor of 50, due to the reduced absorption of the diamond, and allows for *in situ* spin state imaging.

A. Data analysis

The spatial distribution of siderite can be estimated by optical Raman spectroscopy as conventional carbonates have a dominant Raman band ν_1 at ~ 1200 cm^{-1} due to the stretching vibration of the CO₃ group. Integration of the said Raman band leads to a spatial distribution map of siderite. A mapping of intensity of the most intense band around ~ 230 cm^{-1} was used to determine the spatial distribution of the newly formed phases. To obtain information on the crystalline reaction products, we performed XRD imaging of all samples. For the analysis of the diffraction image, DIOPTAS [52] was used. We identified tetrairon(III) orthocarbonate (space group R3c) as well as diiron(II)diiron(III) tetracarbonate (space group C2/c) at different locations in the samples. Afterward, 2- Θ -ranges were selected that exclusively show Bragg reflections of a single compound (see SM for typical diffraction patterns [39]). Mapping of these reflections yields information about the spatial distribution of the corresponding phase, although a quantitative determination of the phase composition was not possible. The spatial distribution of siderite and reaction products derived from mapping of XRD data agree well with the results obtained from the optical Raman spectra. Based on the XES measurements, the average spin state was analyzed by both calculation of the IAD value [40] and compositional fit [13,53] using high-spin and low-spin reference spectra. For both methods, four reference spectra were measured at low and high pressure to cover both high spin and low spin as well as both possible oxidation states Fe²⁺ and Fe³⁺. The samples are listed in Table III and the XES spectra are visualized in Fig. S4 [39]. All spectra were normalized to the area between 7030 eV and 7070 eV and afterward shifted, so the center of mass is at 7055 eV. For the analysis by IAD, the absolute difference to the low-spin reference was calculated and compared to reference spectra. To ensure the spin does not get overrated by low data quality at the rim of the sample, the IAD value was calculated between 7035 eV and 7070 eV. This way, the error of noisy spectra is statistical and not systematical.

To assign the results of the XES maps to the correct phases and obtain information on their spin state, a spin map was calculated based on the XRD mapping. Therefore, the XRD maps for the different phases were broadened to simulate a beam size of 8×8 μm^2 . Afterward, a spin state was assigned to each map. Fe₄C₃O₁₂ is predicted to be in a high-spin state and also to be fully ferric, while Fe₄C₄O₁₃ is predicted to also be in high spin but with a mixture of ferric and ferrous

iron [22,28]. We calculated spin maps for samples A and C based on the XRD map with a spin of 2.5 for $\text{Fe}_4\text{C}_3\text{O}_{12}$ and 2.25 for $\text{Fe}_4\text{C}_4\text{O}_{13}$. The spin state of the siderite map was set to 0. As it is unclear which proportion of each phase is present in the sample based only on the intensity, the different phases have to be weighted by different factors. Figures S6 and S7 (SM) [39] show the impact of different weights on the spin maps. In all maps, the factor for siderite is fixed to 1.

B. Computational details

DFT calculations of iron-containing carbonates are well established (e.g., Ref. [28]). The pressure-induced spin collapse and the change in structure-property relations can be described in a satisfactory manner if an appropriate Hubbard U correction is chosen [28]. First-principles calculations were carried out within the framework of DFT [54], employing the Perdew-Burke-Ernzerhof (PBE) exchange-correlation function [55] and the plane wave/pseudopotential approach implemented in the CASTEP [56] simulation package. On-the-fly ultrasoft and norm-conserving pseudopotentials generated using the descriptors in the CASTEP database were employed in conjunction with plane waves up to a kinetic energy cutoff of 630 eV and 990 eV, respectively. The accuracy of the pseudopotentials is well established [57]. A Monkhorst-Pack [58] grid was used for Brillouin-zone integrations with a distance of $<0.03 \text{ \AA}^{-1}$ between grid points. Most spin-polarized calculations were carried out with a Hubbard U of 2.5 eV for the Fe-atoms. Convergence criteria included an energy change of $<5 \times 10^{-6} \text{ eV atom}^{-1}$, a maximal force of $<0.008 \text{ eV/\AA}$, and a maximal component of the stress tensor $<0.02 \text{ GPa}$. Phonon frequencies were obtained from finite displacement calculations while Raman intensities were

obtained with density functional perturbation theory calculations. However, spin-polarized calculation with an on-site Coulomb repulsion failed to converge for the antiferromagnetic high spin state of $\text{Fe}_4\text{C}_4\text{O}_{13}$.

ACKNOWLEDGMENTS

We acknowledge DESY (Hamburg, Germany), a member of the Helmholtz Association HGF, for the provision of experimental facilities. Parts of this research were carried out at PETRA III beamlines P01 and P02.2. Beamtime was allocated for proposals I-20181129, I-20191002, I-20191008, and I-20200519. We thank Conrad Hagemeyer for technical support at P01, Catherine McCammon and Sergey Lobanov for helpful discussions, and Christian Plückthun for providing a reference sample. We are grateful for gas loading at Deutsches GeoForschungsZentrum and University of Frankfurt and to Rachel Husband and Konstantin Glazyrin for support at P02.2. The FXE-group of XFEL is kindly acknowledged for providing a set of analyzer crystals for use with the von Hamos spectrometer. This work was financially supported by the DFG via STE 1079/4-1, WI1232 and WI 2000/17-1 within the DFG-FOR2125 CarboPaT and STE 1079/2-1. B.W. is grateful for support through the BIOVIA Science Ambassador Program.

C.A., M.T., M.W., and C.St. designed the research. C.A., R.S., L.L., G.S., C.Sch., L.B., N.G., H.G., J.K., H-P.L. M.S., N.T., M.W. and C.St. performed research. C.A. analyzed data with contributions from R.S., J.K. and C.St. B.W. performed calculations, V.C. and S.C. synthesized and provided samples. C.A., B.W., and C.St. wrote the paper with contributions from all coauthors. The authors declare no competing interest.

-
- [1] *Deep Carbon: Past to Present*, edited by Beth N. Orcutt, Isabelle Daniel, and Rajdeep Dasgupta (Cambridge University Press, Cambridge, 2019).
- [2] Y. Fukao, S. Widiyantoro, and M. Obayashi, Stagnant slabs in the upper and lower mantle transition region, *Rev. Geophys.* **39**, 291 (2001).
- [3] M. J. Walter, S. C. Kohn, D. Araujo, G. P. Bulanova, C. B. Smith, E. Gaillou, J. Wang, A. Steele, and S. B. Shirey, Deep mantle cycling of oceanic crust: Evidence from diamonds and their mineral inclusions, *Science* **334**, 54 (2011).
- [4] F. E. Brenker, C. Vollmer, L. Vincze, B. Vekemans, A. Szymanski, K. Janssens, I. Szaloki, L. Nasdala, W. Joswig, and F. Kaminsky, Carbonates from the lower part of transition zone or even the lower mantle, *Earth Planet. Sci. Lett.* **260**, 1 (2007).
- [5] F. Kaminsky, Mineralogy of the lower mantle: A review of ‘super-deep’ mineral inclusions in diamond, *Earth-Sci. Rev.* **110**, 127 (2012).
- [6] A. R. Thomson, S. C. Kohn, G. P. Bulanova, C. B. Smith, D. Araujo, EIMF, and M. J. Walter, Origin of sub-lithospheric diamonds from the Juina-5 kimberlite (Brazil): Constraints from carbon isotopes and inclusion compositions, *Contrib. Mineral. Petrol.* **168**, 1081 (2014).
- [7] J. F. Lin, J. Liu, C. Jacobs, and V. B. Prakapenka, Vibrational and elastic properties of ferromagnesite across the electronic spin-pairing transition of iron, *Am. Mineral.* **97**, 583 (2012).
- [8] G. Farfan, S. Wang, H. Ma, R. Caracas, and W. L. Mao, Bonding and structural changes in siderite at high pressure, *Am. Mineral.* **97**, 1421 (2012).
- [9] V. Cerantola, C. McCammon, I. Kupenko, I. Kantor, C. Marini, M. Wilke, L. Ismailova, N. Solopova, A. Chumakov, S. Pascarelli, and L. Dubrovinsky, High-pressure spectroscopic study of siderite (FeCO_3) with a focus on spin crossover, *Am. Mineral.* **100**, 2670 (2015).
- [10] J. Müller, S. Speziale, I. Efthimiopoulos, S. Jahn, and M. Koch-Müller, Raman spectroscopy of siderite at high pressure: Evidence for a sharp spin transition, *Am. Mineral.* **101**, 2638 (2016).
- [11] C. Weis, C. Sternemann, V. Cerantola, C. J. Sahle, G. Spiekermann, M. Harder, Y. Forov, A. Kononov, R. Sakrowski, H. Yavaş, M. Tolan, and M. Wilke, Pressure driven spin transition in siderite and magnesiosiderite single crystals, *Sci. Rep.* **7**, 16526 (2017).
- [12] V. Cerantola, M. Wilke, I. Kantor, L. Ismailova, I. Kupenko, C. McCammon, S. Pascarelli, and L. S. Dubrovinsky, Experimental investigation of FeCO_3 (siderite) stability in Earth’s lower mantle using XANES spectroscopy, *Am. Mineral.* **104**, 1083 (2019).

- [13] C. Weis, G. Spiekermann, C. Sternemann, M. Harder, G. Vankó, V. Cerantola, C. J. Sahle, Y. Forov, R. Sakrowski, I. Kupenko, S. Petitgirard, H. Yavaş, C. Bressler, W. Gawelda, M. Tolan, and M. Wilke, Combining x-ray $K\beta_{1,3}$, valence-to-core, and x-ray Raman spectroscopy for studying Earth materials at high pressure and temperature: The case of siderite, *J. Anal. At. Spectrom.* **34**, 384 (2019).
- [14] M. Stekiel, A. Girard, T. Nguyen-Thanh, A. Bosak, V. Milman, and B. Winkler, Phonon-driven phase transitions in calcite, dolomite, and magnesite, *Phys. Rev. B* **99**, 054101 (2019).
- [15] J. Binck, S. Chariton, M. Stekiel, L. Bayarjargal, W. Morgenroth, V. Milman, L. Dubrovinsky, and B. Winkler, High-pressure, high-temperature phase stability of iron-poor dolomite and the structures of dolomite-IIIc and dolomite-V, *Phys. Earth Planet. Inter.* **299**, 106403 (2020).
- [16] A. R. Oganov, S. Ono, Y. Ma, C. W. Glass, and A. Garcia, Novel high-pressure structures of $MgCO_3$, $CaCO_3$ and CO_2 and their role in Earth's lower mantle, *Earth Planet. Sci. Lett.* **273**, 38 (2008).
- [17] E. Boulard, A. Gloter, A. Corgne, D. Antonangeli, A.-L. Auzende, J.-P. Perrillat, F. Guyot, and G. Fiquet, New host for carbon in the deep Earth, *Proc. Nat. Acad. Sci. USA* **108**, 5184 (2011).
- [18] E. Boulard, N. Menguy, A. L. Auzende, K. Benzerara, H. Bureau, D. Antonangeli, A. Corgne, G. Morard, J. Siebert, J. P. Perrillat, F. Guyot, and G. Fiquet, Experimental investigation of the stability of Fe-rich carbonates in the lower mantle, *J. Geophys. Res.: Solid Earth* **117**, B02208 (2012).
- [19] E. Boulard, D. Pan, G. Galli, Z. Liu, and W. L. Mao, Tetrahedrally coordinated carbonates in Earth's lower mantle, *Nat. Commun.* **6**, 6311 (2015).
- [20] J. Liu, J. F. Lin, and V. B. Prakapenka, High-pressure orthorhombic ferromagnesite as a potential deep-mantle carbon carrier, *Sci. Rep.* **5**, 7640 (2015).
- [21] M. Merlini, M. Hanfland, A. Salamat, S. Petitgirard, and H. Müller, The crystal structures of $Mg_2Fe_2C_4O_{13}$, with tetrahedrally coordinated carbon, and $Fe_{13}O_{19}$, synthesized at deep mantle conditions, *Am. Mineral.* **100**, 2001 (2015).
- [22] V. Cerantola, E. Bykova, I. Kupenko, M. Merlini, L. Ismailova, C. McCammon, M. Bykov, A. I. Chumakov, S. Petitgirard, I. Kantor, V. Svitlyk, J. Jacobs, M. Hanfland, M. Mezouar, C. Prescher, R. Rüffer, V. B. Prakapenka, and L. Dubrovinsky, Stability of iron-bearing carbonates in the deep Earth's interior, *Nat. Commun.* **8**, 15960 (2017).
- [23] M. Merlini, V. Cerantola, G. D. Gatta, M. Gemmi, M. Hanfland, I. Kupenko, P. Lotti, H. Müller, and L. Zhang, Dolomite-IV: Candidate structure for a carbonate in the Earth's lower mantle, *Am. Mineral.* **102**, 1763 (2017).
- [24] D. Laniel, J. Binck, B. Winkler, S. Vogel, T. Fedotenko, S. Chariton, V. Prakapenka, V. Milman, W. Schnick, L. Dubrovinsky, and N. Dubrovinskaia, Synthesis, crystal structure and structure-property relations of strontium orthocarbonate, Sr_2CO_4 , *Acta Crystallogr. Sect. B* **77**, 131 (2021).
- [25] D. Spahr, J. Binck, L. Bayarjargal, R. Luchitskaia, W. Morgenroth, D. Comboni, V. Milman, and B. Winkler, Tetrahedrally coordinated sp^3 -hybridized carbon in Sr_2CO_4 orthocarbonate at ambient conditions, *Inorg. Chem.* **60**, 5419 (2021).
- [26] B. Lavina, P. Dera, R. T. Downs, W. Yang, S. Sinogeikin, Y. Meng, G. Shen, and D. Schiferl, Structure of siderite $FeCO_3$ to 56 GPa and hysteresis of its spin-pairing transition, *Phys. Rev. B* **82**, 064110 (2010).
- [27] E. Bykova, L. Dubrovinsky, N. Dubrovinskaia, M. Bykov, C. McCammon, S. V. Ovsyannikov, H. P. Liermann, I. Kupenko, A. I. Chumakov, R. Rüffer, M. Hanfland, and V. Prakapenka, Structural complexity of simple Fe_2O_3 at high pressures and temperatures, *Nat. Commun.* **7**, 10661 (2016).
- [28] Z. Li and S. Stackhouse, Iron-rich carbonates stabilized by magnetic entropy at lower mantle conditions, *Earth Planet. Sci. Lett.* **531**, 115959 (2020).
- [29] J. Badro, G. Fiquet, F. Guyot, J. P. Rueff, V. V. Struzhkin, G. Vankó, and G. Monaco, Iron partitioning in Earth's mantle: Toward a deep lower mantle discontinuity, *Science* **300**, 789 (2003).
- [30] D. J. Frost, C. Liebske, F. Langenhorst, C. A. McCammon, R. G. Trønnes, and D. C. Rubie, Experimental evidence for the existence of iron-rich metal in the Earth's lower mantle, *Nature (London)* **428**, 409 (2004).
- [31] C. McCammon, The paradox of mantle redox, *Science* **308**, 807 (2005).
- [32] D. J. Frost and C. A. McCammon, The redox state of Earth's mantle, *Annu. Rev. Earth Planet Sci.* **36**, 389 (2008).
- [33] I. Kupenko, C. McCammon, R. Sinmyo, V. Cerantola, V. Potapkin, A. I. Chumakov, A. Kantor, R. Rüffer, and L. Dubrovinsky, Oxidation state of the lower mantle: *In situ* observations of the iron electronic configuration in bridgmanite at extreme conditions, *Earth Planet. Sci. Lett.* **423**, 78 (2015).
- [34] H. Piet, J. Badro, F. Nabeii, T. Dennenwaldt, S. H. Shim, M. Cantoni, C. Hébert, and P. Gillet, Spin and valence dependence of iron partitioning in Earth's deep mantle, *Proc. Nat. Acad. Sci. USA* **113**, 11127 (2016).
- [35] I. Mashino, M. Murakami, N. Miyajima, and S. Petitgirard, Experimental evidence for silica-enriched Earth's lower mantle with ferrous iron dominant bridgmanite, *Proc. Nat. Acad. Sci. USA* **117**, 27899 (2020).
- [36] T. Irifune, T. Shinmei, C. A. McCammon, N. Miyajima, D. C. Rubie, and D. J. Frost, Iron partitioning and density changes of pyrolite in Earth's lower mantle, *Science* **327**, 193 (2010).
- [37] R. Sinmyo and K. Hirose, Iron partitioning in pyrolitic lower mantle, *Phys. Chem. Miner.* **40**, 107 (2013).
- [38] C. Prescher, F. Langenhorst, L. S. Dubrovinsky, V. B. Prakapenka, and N. Miyajima, The effect of Fe spin crossovers on its partitioning behavior and oxidation state in a pyrolitic Earth's lower mantle system, *Earth Planet. Sci. Lett.* **399**, 86 (2014).
- [39] See Supplemental Material at <http://link.aps.org/supplemental/10.1103/PhysRevB.105.085155> for information on the DAC preparation, the laser heating process, data analysis, and additional data related to the paper.
- [40] G. Vankó, T. Neisius, G. Molnár, F. Renz, S. Kárpáti, A. Shukla, and F. M. de Groot, Probing the 3D spin momentum with x-ray emission spectroscopy: The case of molecular-spin transitions, *J. Phys. Chem. B* **110**, 11647 (2006).
- [41] Q. Hu, D. Y. Kim, W. Yang, L. Yang, Y. Meng, L. Zhang, and H. K. Mao, FeO_2 and $FeOOH$ under deep lower-mantle conditions and Earth's oxygen-hydrogen cycles, *Nature (London)* **534**, 241 (2016).
- [42] M. Murakami, K. Hirose, N. Sata, and Y. Ohishi, Post-perovskite phase transition and mineral chemistry in the

- pyrolitic lowermost mantle, *Geophys. Res. Lett.* **32**, 3 (2005).
- [43] S. H. Shim, B. Grocholski, Y. Ye, E. E. Alp, S. Xu, D. Morgan, Y. Meng, and V. B. Prakapenka, Stability of ferrous-iron-rich bridgmanite under reducing midmantle conditions, *Proc. Nat. Acad. Sci. USA* **114**, 6468 (2017).
- [44] R. Huang, T. Boffa Ballaran, C. A. McCammon, N. Miyajima, D. Dolejš, and D. J. Frost, The composition and redox state of bridgmanite in the lower mantle as a function of oxygen fugacity, *Geochim. Cosmochim. Acta* **303**, 110 (2021).
- [45] R. Sinmyo and K. Hirose, The Soret diffusion in laser-heated diamond-anvil cell, *Phys. Earth Planet. Inter.* **180**, 172 (2010).
- [46] Y. Akahama and H. Kawamura, Pressure calibration of diamond anvil Raman gauge to 310 GPa, *J. Appl. Phys.* **100**, 043516 (2006).
- [47] S. Petitgirard, G. Spiekermann, C. Weis, C. Sahle, C. Sternemann, and M. Wilke, Miniature diamond anvils for x-ray Raman scattering spectroscopy experiments at high pressure, *J. Synchrotron Radiat.* **24**, 276 (2017).
- [48] I. Kantor, V. Prakapenka, A. Kantor, P. Dera, A. Kurnosov, S. Sinogeikin, N. Dubrovinskaia, and L. Dubrovinsky, BX90: A new diamond anvil cell design for x-ray diffraction and optical measurements, *Rev. Sci. Instrum.* **83**, 125102 (2012).
- [49] G. Spiekermann, I. Kuppenko, S. Petitgirard, M. Harder, A. Nyrow, C. Weis, C. Albers, N. Biedermann, L. Libon, C. J. Sahle, V. Cerantola, K. Glazyrin, Z. Konôpková, R. Sinmyo, W. Morgenroth, I. Sergueev, H. Yavaş, L. Dubrovinsky, M. Tolan, C. Sternemann, and M. Wilke, A portable on-axis laser-heating system for near-90° x-ray spectroscopy: Application to ferropericlase and iron silicide, *J. Synchrotron Radiat.* **27**, 414 (2020).
- [50] R. Alonso-Mori, J. Kern, D. Sokaras, T. C. Weng, D. Nordlund, R. Tran, P. Montanez, J. Delor, V. K. Yachandra, J. Yano, and U. Bergmann, A multi-crystal wavelength dispersive x-ray spectrometer, *Rev. Sci. Instrum.* **83**, 073114 (2012).
- [51] J. Szlachetko, M. Nachtegaal, E. de Boni, M. Willmann, O. Safonova, J. Sa, G. Smolentsev, M. Szlachetko, J. A. Van Bokhoven, J. C. Dousse, J. Hozzowska, Y. Kayser, P. Jagodzinski, A. Bergamaschi, B. Schmitt, C. David, and A. Lücke, A von Hamos x-ray spectrometer based on a segmented-type diffraction crystal for single-shot x-ray emission spectroscopy and time-resolved resonant inelastic x-ray scattering studies, *Rev. Sci. Instrum.* **83**, 103105 (2012).
- [52] C. Prescher and V. B. Prakapenka, DIOPTAS: A program for reduction of two-dimensional x-ray diffraction data and data exploration, *High Press. Res.* **35**, 223 (2015).
- [53] J. Badro, J. P. Rueff, G. Vankó, G. Monaco, G. Fiquet, and F. Guyot, Electronic transitions in perovskite: Possible nonconducting layers in the lower mantle, *Science* **305**, 383 (2004).
- [54] P. Hohenberg and W. Kohn, Inhomogeneous electron gas, *Phys. Rev.* **136**, B864 (1964).
- [55] J. P. Perdew, K. Burke, and M. Ernzerhof, Generalized Gradient Approximation Made Simple, *Phys. Rev. Lett.* **77**, 3865 (1996).
- [56] S. J. Clark, M. D. Segall, C. J. Pickard, P. J. Hasnip, M. I. Probert, K. Refson, and M. C. Payne, First principles methods using CASTEP, *Z. Kristallogr.* **220**, 567 (2005).
- [57] K. Lejaeghere, G. Bihlmayer, T. Björkman, P. Blaha, S. Blügel, V. Blum, D. Caliste, I. E. Castelli, S. J. Clark, A. Dal Corso, S. De Gironcoli, T. Deutsch, J. K. Dewhurst, I. Di Marco, C. Draxl, M. Dułak, O. Eriksson, J. A. Flores-Livas, K. F. Garrity, L. Genovese *et al.*, Reproducibility in density functional theory calculations of solids, *Science* **351**, aad3000 (2016).
- [58] H. J. Monkhorst and J. D. Pack, Special points for Brillouin-zone integrations, *Phys. Rev. B* **13**, 5188 (1976).